RESEARCH ARTICLE

Magnetic Resonance in Medicine

Referenceless Nyquist ghost correction outperforms standard navigator-based method and improves efficiency of in vivo diffusion tensor cardiovascular magnetic resonance

Zimu Huo[1,2] | **Ke Wen**[1,3] | **Yaqing Luo**[1,3] | **Radhouene Neji**[4] | **Karl P. Kunze**[4] | **Pedro F. Ferreira**[1,3] | **Dudley J. Pennell**[1,3] | **Andrew D. Scott**[1,3] | **Sonia Nielles-Vallespin**[1,3]

[1]CMR Unit, Royal Brompton Hosptial, Guy's and St Thomas' NHS Foundation Trust, London, UK

[2]Department of Bioengineering, Imperial College London, London, UK

[3]NHLI, Imperial College London, London, UK

[4]MR Research Collaborations, Siemens Healthcare Limited, Camberley, UK

Correspondence
Andrew D. Scott, CMR Unit, Royal Brompton Hosptial, Guy's and St Thomas' NHS Foundation Trust, Sydney St, London SW3 6NP, UK.
Email: a.scott07@imperial.ac.uk

Funding information
British Heart Foundation, Grant/Award Number: RG/19/1/34160

Abstract

Purpose: The study aims to assess the potential of referenceless methods of EPI ghost correction to accelerate the acquisition of in vivo diffusion tensor cardiovascular magnetic resonance (DT-CMR) data using both computational simulations and data from in vivo experiments.

Methods: Three referenceless EPI ghost correction methods were evaluated on mid-ventricular short axis DT-CMR spin echo and STEAM datasets from 20 healthy subjects at 3T. The reduced field of view excitation technique was used to automatically quantify the Nyquist ghosts, and DT-CMR images were fit to a linear ghost model for correction.

Results: Numerical simulation showed the singular value decomposition (SVD) method is the least sensitive to noise, followed by Ghost/Object method and entropy-based method. In vivo experiments showed significant ghost reduction for all correction methods, with referenceless methods outperforming navigator methods for both spin echo and STEAM sequences at $b = 32$, 150, 450, and 600 smm^{-2}. It is worth noting that as the strength of the diffusion encoding increases, the performance gap between the referenceless method and the navigator-based method diminishes.

Conclusion: Referenceless ghost correction effectively reduces Nyquist ghost in DT-CMR data, showing promise for enhancing the accuracy and efficiency of measurements in clinical practice without the need for any additional reference scans.

KEYWORDS
EPI artifacts, Nyquist ghost, SE-EPI

Andrew D. Scott and Sonia Nielles-Vallespin contributed equally to this work.

1 | INTRODUCTION

Diffusion tensor cardiovascular magnetic resonance (DT-CMR) allows noninvasive interrogation of the myocardium at a microscopic level and typically relies on single-shot echo planar imaging (EPI) acquisitions.[1] Due to the alternating direction of the EPI readout lines, hardware imperfections such as timing delays, eddy currents, and gradient coil heating can cause misalignment of the forward and reverse lines in K-space. This misalignment manifests itself in the images as a Nyquist (N/2) ghost in the phase encoding direction and sinusoidal modulation of the object in the frequency encode direction.[2] If left uncorrected, the ghost artifacts reduce image quality and compromise the image signal-to-noise ratio (SNR), which would lead to errors in the quantitative measurements in DT-CMR parameters, such as mean diffusivity (MD), fractional anisotropy (FA), and the second eigenvector angle (E2A).[3]

The EPI readouts used in DT-CMR applications typically rely on separately acquired phase correction navigators to measure the difference between alternating readout polarity, which is modeled as a linear phase error.[2] Although this well-established method works well in the brain, it can be less effective in cardiac imaging because of increased susceptibility at the heart–lung tissue interface and motion at the chest wall[4] and requires additional data acquisition which can be time consuming. Several other ghost correction methods have been proposed including acquiring a full 2D reference scan,[5–7] coordinate encoding (PLACE),[8] annihilating filter-based,[9] and parallel imaging-based techniques.[10–14] In contrast to methods which use separately acquired data to minimize EPI misalignment induced artifacts, referenceless methods use data-driven techniques for self-correction,[15–18] extracting the misalignment information directly from the acquired imaging data. These referenceless methods integrate various prior knowledge sources to mitigate Nyquist ghost artifacts using a cost function that is minimized when the ghost is suppressed. The entropy-based method attempts to minimize the image entropy of the magnitude image to minimize EPI misalignment artifacts.[15,17] The singular value decomposition (SVD) method defines a cost function based on enforcing the self-consistency of neighboring K-space points,[18] while the Ghost/Object method tries to minimize the overlap between the imaged object and ghost.[16] Referenceless methods are potentially advantageous due to their time efficiency, as they do not require additional reference scans. This is particularly relevant in DT-CMR applications as data must be acquired within short windows that align with the peak systole or during diastasis when cardiac motion is minimal. Additionally, the scan time is limited by the subject's

RR interval, making referenceless methods a compelling option for reducing the number and duration of breath holds and optimizing the scanning process.[19,20] So far, limited research has been conducted to fully assess the effectiveness of these data-driven, referenceless methods in practice, considering factors such as SNR, diffusion weighting, and resolution of DT-CMR data.[1]

In this work, we will evaluate entropy-based, SVD-based, and Ghost/Object minimization in application to DT-CMR. We will investigate and compare the performance of these techniques to a standard navigator-based EPI phase correction method. Noise sensitivity of the methods will be first assessed using a computational simulation with a digital phantom. The performance of these referenceless methods will then be evaluated using in vivo DT-CMR data.

2 | THEORY

2.1 | Linear ghost model

Hardware imperfections can cause a slight deviation between otherwise equivalent points along the frequency encoding axis between even and odd echoes in the EPI readout. Such misalignment of the echoes in K-space leads to an artifact known as Nyquist ghosting, that is, the image acquired will be a superposition of the true image and a copy shifted by half of the field of view (FOV) in the phase encoding (PE) direction.[21] Moreover, a cosine modulation of the signal intensities will occur in the frequency encoding direction.

The misalignment between the forward and reverse kx lines is usually modeled as a linear phase difference in the hybrid space (after Fourier transforming the data along the frequency encoding axis) as follows[21]:

$$S\left(x, k_{y_{odd}}\right) = e^{i\left(\frac{\pi\alpha}{N_x}x + \beta\right)}, \tag{1}$$

where x is the index of the position in the readout direction of total size N_x, α is the slope of the phase due to the constant time echo delay and β is a constant off-resonance phase shift between the even and odd readouts in K-space. An example simulation showing the effect of the two phase error parameters is shown in Figure 1.

2.2 | Navigator-based correction

Nyquist ghosts are commonly corrected using a three-line EPI readout performed without PE, known as a phase-navigator. The three lines each pass through the center of K-space to acquire reference echoes with different
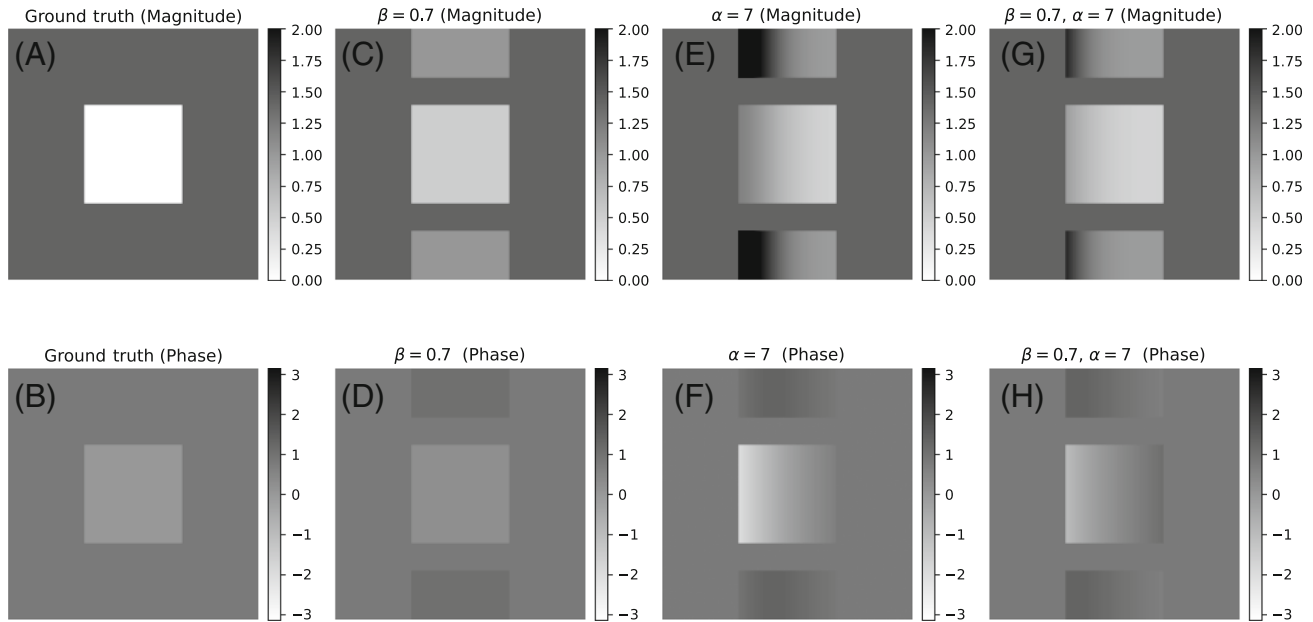
FIGURE 1 Overview of the effects of the parameters in the linear phase Nyquist ghost model on the image space data using a numerical phantom. The white box in the image has a size of 100 by 100 pixels, and it is centered within the image, which has a size of 256 by 256 pixels. The vertical axis of the image represents the phase encoding direction. The top row shows the magnitude images, and the bottom row shows the phase images. (A) The ground truth image. (B) Phase image of the ground truth phantom. In (C) and (D), a phase offset β was added to the image. The ghost resulted in a shifted copy of the original object being observed at the half field of view (FOV) position in the phase encoding direction, and the overall intensity of the parent object decreases. In (E) and (F), A linear phase error α was added to every odd line in K-space resulting in cosine modulation of the signal intensities in the frequency encoding direction in addition to the half FOV ghost. The cosine modulation is also present in the phase image. In (G) and (H), the examples combine the two phase error parameters to show their combined effects on the image amplitude and phase.

polarities: S1+, S2−, S3+.[2] Here the plus and minus sign denotes the gradient polarity of the readout gradient in the EPI pulse train. By averaging the reference echo S1+ and reference echo S3+, a pseudo interpolated reference echo S2+ can be generated as if the second reference echo is collected with positive gradient polarity. The linear phase model (Equation 1) is then fitted to the phase of the difference between the reference echo S2− and the interpolated S2+ in the hybrid space.

2.3 | Referenceless correction methods

In this work, we compared three referenceless correction methods in application to DT-CMR: entropy-based, SVD-based, and the Ghost/Object minimization method. Similar to that of the three-line navigator-based phase correction, the referenceless methods attempt to identify the most suitable phase correction parameters by minimizing a cost function. In contrast to traditional methods using reference echoes, referenceless techniques rely on an exhaustive search of potential model parameters to optimize the correction. The effectiveness of each of these parameter speculations is then evaluated based on

their ability to improve the quality of the phase corrected images, as determined by specific, predefined metrics. The following are the three methods evaluated:

1. Entropy-based method: The cost function for the entropy-based method relies on the traditional image entropy measure of the magnitude image in the spatial domain.[15,22]
2. SVD-based method: For the SVD-based phase correction, the K-space multicoil channels are reformatted into block-wise Hankel matrix structure with each row being flattened slice-GRAPPA kernels before performing SVD.[18,23–25] The cost of using the SVD method is determined by the sum of the singular values within a user-defined range based on the estimation of the rank of the Hankel structure. This range, known as the minimization zone, extends from the estimated rank n of the matrix to the end of the singular values N.
3. Ghost/Object minimization method: For the Ghost/Object minimization strategy,[16] the cost function is defined by equation 2:

$$f^{-1} = \sum_{x,y} F_{\text{med2D}} \frac{|I_{x,y}|}{|I'_{x,y}|}, \tag{2}$$

where F is the 2D median filter, I is the measure image in image space (x, y), and I' is the copy of I shifted by half FOV in the PE direction. Following this expression, the cost is computed by taking the ratio of the magnitude image over the shifted copy at the half FOV position in the PE direction to measure the signal-to-ghost overlap. To eliminate noise and outliers, a 2D median filter is applied, as these can distort the calculation by adding excessive/insufficient values. The cost is then computed by taking the reciprocal of the magnitude sum over the entire image.

3 | METHODS

3.1 | Simulation

To compare the performance of the referenceless methods, a set of numerical phantoms based on a 2D short axis image in the mid-ventricle with known DT-CMR parameters, including FA, MD, HA, and E2A, were generated in MATLAB (The Mathworks). The simulation parameters are as follows: left ventricular myocardial thickness 16 mm, left ventricle blood pool radius 16 mm, sampling size 96 by 256 mm². The numerical phantoms were based on a heart in peak systole with 10 repetitions at $b = 0 \, \text{s} \, \text{mm}^{-2}$, followed by six diffusion encoding directions and two repetitions at $b = 150 \, \text{s} \, \text{mm}^{-2}$ and eight repetitions with 600 $\text{s} \, \text{mm}^{-2}$ to match the standard in vivo acquisition protocol (70 images per set). The coil sensitivity maps, corresponding to a 16-channel receive array, are generated using the Michigan Image Reconstruction Toolbox (MIRT).[26]

The imaging techniques employed in this work involved a reduced FOV in the phase encode direction, allowing the relative ghost level to be measured using the signal outside this excited region as a measure of the artifact level as shown in Figure 2. More details are provided in the in vivo data acquisition section.

This study commences by investigating the Nyquist ghost magnitude in relation to SNR, while also considering its dependence on parameters α and β. We introduced complex white Gaussian noise resulting in SNR values of 1, 5, and 10 for the simulated heart phantom. The EPI phase error was systematically varied within practical limits, where α ranged from 0 to 10 with an increment of 0.2, and β ranged from 0 to 1 with an increment of 0.02. Subsequently, these resulting images underwent evaluation using five distinct metrics: root mean square error (RMSE), level of artifact (artifact quantification through the reduced FOV), entropy cost, Ghost/Object cost, and SVD cost. This entire process was iterated 50 times to compute the mean.

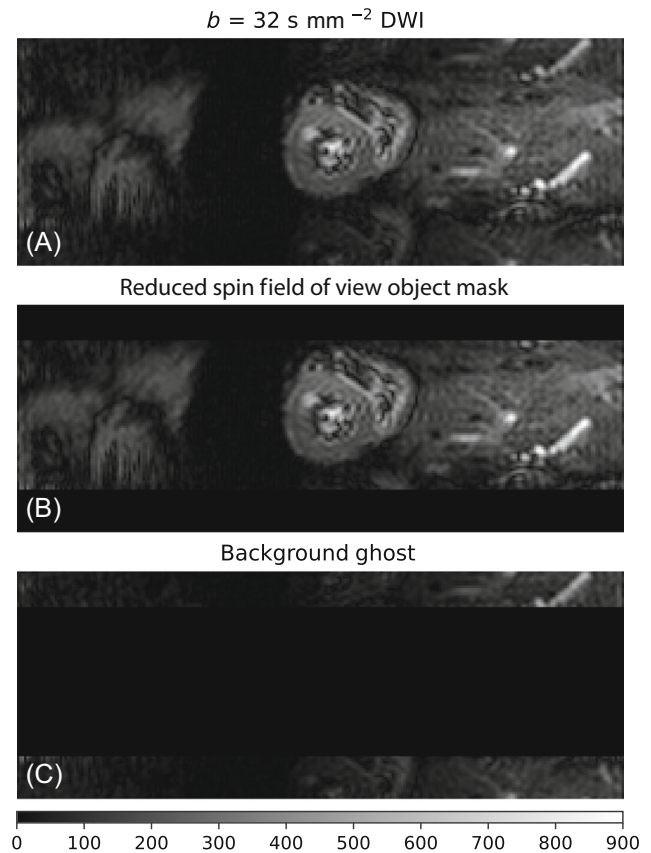In the second experiment, the performance of the Nyquist ghost correction methods was evaluated. The

$b = 32 \, \text{s} \, \text{mm}^{-2}$ DWI

Reduced spin field of view object mask

Background ghost

| 0 | 100 | 200 | 300 | 400 | 500 | 600 | 700 | 800 | 900 |

FIGURE 2 Measurement of the Nyquist ghosts. This example (A) highlights the Nyquist ghost for the uncorrected b0 image. The image (B) shows the mask which separates the object and ghost. The image (C) shows the residual ghost outside the reduced field of view. The level of ghosting is measured by the sum of the magnitude image outside the reduced field of view.

phantom was modified by adding complex white Gaussian distributed noise to the K-space data to simulate 20 different SNRs before applying the phase error. For each simulation repetition, the phase error was randomly selected from uniform distributions within practicable ranges $-10 < \alpha < 10$ and $-1 < \beta < 1$ then a small perturbation $-0.03 < \epsilon < 0.03$ was added to the phase offset and slope for each diffusion encoding direction and repetition to simulate physiologically induced off-resonance effects. A brute-force search over the 2D space of phase slopes in the range -10 to 10 (step size 0.2) and phase offsets in the range -1 to 1 (step size 0.02) was used to find the optimal phase correction offset and slope parameters using the three referenceless cost functions computed on the noisy DT-CMR numerical phantom images. The error was measured using the Euclidean distance between the ideal images and the phase-corrected images averaged over 50 trials for each SNR level. It is important to note that the navigator-based method cannot be simulated using the methodology described in this work,

as it would result in an inverse crime where the same model is used for both generating the simulated data and the subsequent reconstruction. It would also consistently yield accurate α and β parameters and therefore a perfectly ghost-corrected image, which is not representative of the true performance of navigator methods in vivo.

3.2 | In vivo data acquisition

A reduced FOV method can be implemented using the in-plane selective RF pulses. In this case, a large portion of the Nyquist ghost will fall outside the field of view which generates the spin or stimulated echo, enabling a surrogate measurement of the ghost level. In our acquisitions, this region which does not contribute to imaging signal in the PE direction, will account for 20% of the entire image. We assumed perfect reduced FOV and defined the ghost level as the sum of the magnitude image outside the reduced FOV as shown in Figure 2.

DT-CMR data were acquired in a mid-ventricular short axis slice in peak systole during breath holding using a motion compensated Spin Echo (SE) and STimulated Echo Acquisition Mode (STEAM) single-shot EPI research sequence from 20 healthy volunteers.[19,20] Images were acquired with a clinical 3T scanner (MAGNETOM Vida, Siemens Healthcare) with 60 mT m^{-1} maximum gradient strength, 200T/m/s slew rate, using a 12-channel posterior spine array and 18-channel flexible anterior array. The "b0" image was acquired with b $\approx$ 32 s mm^{-2} for STEAM followed by six diffusion encoding directions with two repetitions at $b = 150$ s mm^{-2} and 8 to 10 repetitions at 450 and 600 s mm^{-2} for SE and STEAM, respectively. Imaging parameters are as follows: TE$_{SE}$ = 62 ms and TE$_{STEAM}$ = 22 ms, TR = 2 cardiac cycles, field of view 360 by 135 mm^2 (reduced phase FOV), 2442 Hz/pixel bandwidth, 2.8 by 2.8 mm^2 resolution or 1.4 by 1.4 mm^2 reconstructed with zero padding, ×2 undersampling for parallel imaging, and no partial Fourier used. A three-line EPI phase correction navigator was acquired at the beginning of each breath hold with PE disabled (as either a SE or STEAM, matching the imaging data).

3.3 | Reconstruction and Nyquist ghost correction

The in vivo raw data were reconstructed using five methods: (1) Uncorrected images, (2) Navigator-based correction, (3) Entropy method, (4) SVD method, (5) Ghost/Object minimization method. We employed an average coil, per slice, per acquisition technique to effectively reduce the Nyquist ghost levels with low SNRs for all referenceless methods.

(1) Uncorrected. The GRAPPA[27] kernels, size 4 by 5 in PE and frequency encoding directions, were first trained on the uncorrected parallel imaging reference scan and used to reconstruct the data without phase correction to provide an "uncorrected" Nyquist ghost baseline measurement.

(2) Navigator-based method. The linear phase difference was extracted using a Savitzky–Golay filtered first-order fit weighted by the one-dimensional object projection of the object in the hybrid space. This allowed the determination of the Nyquist ghost correction parameters α and β. The phase offset and slope were then applied to the parallel imaging reference scan and aliased data, and a GRAPPA reconstruction with the same kernel parameters as for (1) was applied subsequently.

(3) Entropy-based method. A brute-force search was used to find the phase correction offset and slope using the image entropy cost function computed on the low-resolution parallel imaging reference scan by finding the global minimum. The Nyquist ghost correction parameters α and β providing this minimum entropy were then applied to the parallel imaging reference scan to obtain low-resolution ghost-free calibration data. This corrected calibration data was then used with the undersampled imaging data to perform a secondary brute force search for the ghost correction parameters corresponding to the minimum entropy on each coil-combined image to account for any physiological and physical-induced phase errors between consecutive EPI shots.

(4) SVD-based method. Reconstruction as for method 3 except for the cost function. The multicoil data was first reformatted into a Hankel matrix. The number of rows in the matrix was determined by the size of the GRAPPA kernel, while the number of columns corresponded to the number of GRAPPA kernels or the number of convolutions. Thus, each row of the Hankel matrix was a flattened 3 by 3 GRAPPA-like kernel. Then a SVD was performed on the large Hankel matrix, generating a set of singular values as the basis for the minimization problem. Finally, the cost function was determined by the summation of all the singular values except the principle/largest one and the selected phase correction parameters were chosen based on a brute force search for the minimum cost function (for the parallel imaging reference data and then the imaging data).

(5) Ghost/Object minimization method. Reconstruction as per method 4 using the Ghost/Object cost function.

The cost function was defined by Equation (2) and following this definition, an overlap measure was first calculated as the ratio of the coil-combined magnitude image over the shifted copy at the half FOV position in the PE direction, followed by a 3 by 3 2D median filter to remove noise and outliers. The cost function was computed by taking the reciprocal of the magnitude sum over this median filtered overlap measure.

All corrections were processed offline in Python and the SVD-based method was implemented in TensorFlow to accelerate the SVD. The DT-CMR data was processed using in-house MATLAB software.

In the in vivo experiment, we conducted pairwise comparisons of the EPI ghost for navigator based method and each of the EPI referenceless methods for two sequences at various diffusion weightings to identify statistical differences. We used a p-value threshold of 0.05 for these comparisons. The results allowed us to determine if there are significant differences between the navigator-based correction and the referenceless methods. To quantify the difference in DT-CMR parameters, we used difference in the mean FA, difference in the mean MD, and difference in the median of the absolute value of E2A.

4 | RESULTS

Figure 3 shows the RMSE, level of artifact, entropy cost, Ghost/Object cost, and SVD cost as a function of α and β at three SNR levels when using the digital heart phantom as the source image. Across all SNR levels, the cost functions for the referenceless methods consistently identify regions with low β and low α values as having minimal ghosting, aligning with the RMSE contour plot.

One single realization of the Monte Carlo DT-CMR simulation is shown in Figure 4. In this example, the SVD-based ghost correction successfully suppressed the Nyquist ghosting. Example DT-CMR maps from simulated data are shown in Figure 5 with an SNR of 5. Upon visual inspection, it was observed that all methods effectively suppressed the EPI ghost; however, the Ghost/Object minimization method and SVD-based method exhibited less susceptibility to noise compared to the entropy-based method.

The overall performance of the Nyquist ghost correction methods is shown in Figure 6. As indicated in Part B, the SVD was the least sensitive to noise, followed by Ghost/Object method, and finally entropy-based method. The numerical phantom data were used to calculate MD
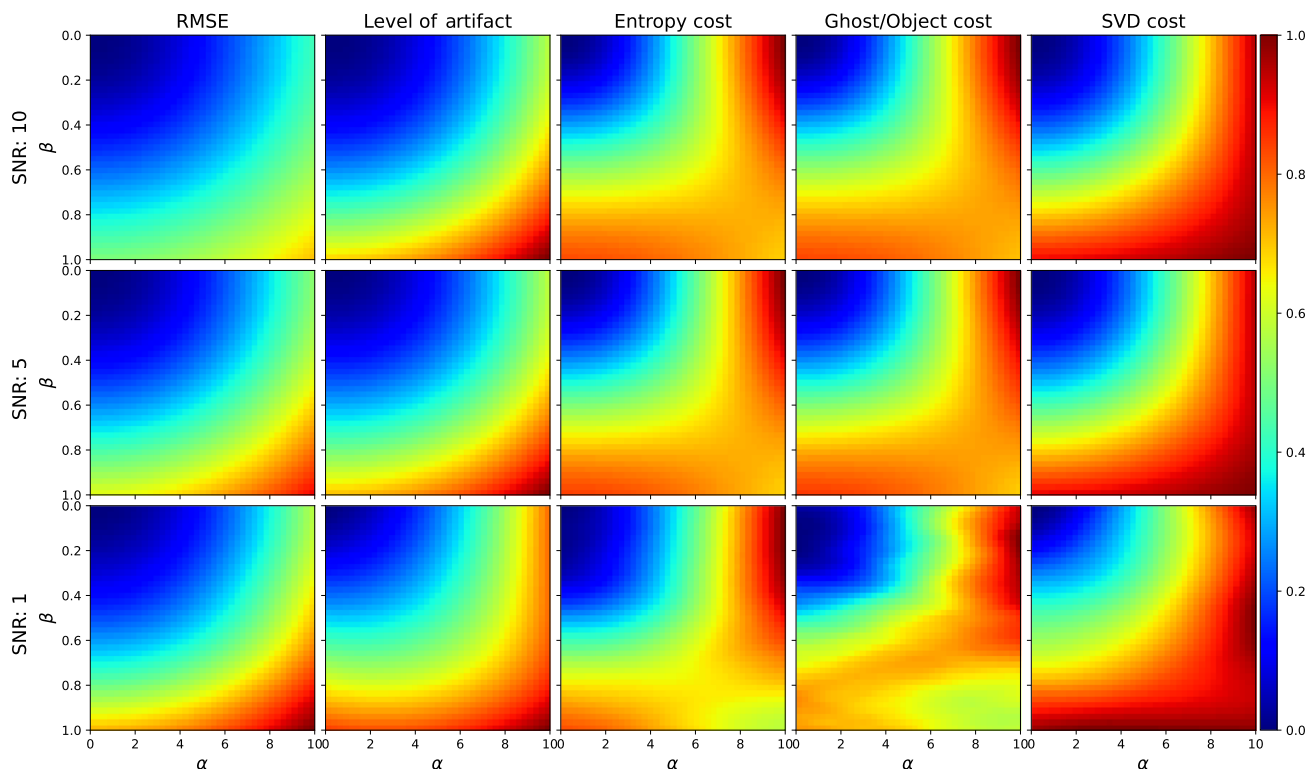

FIGURE 3 Cost contour plot for root mean square error (RMSE), level of artifact, entropy cost, Ghost/Object cost, and singular value decomposition (SVD) cost as a function of α and β at three signal-to-noise ratio levels. For the RMSE and level of artifact plot, values are normalized using the maximum value within their respective columns. The contour plots for the cost functions are individually normalized between 0 and 1. The referenceless methods work by computing such contour plots and finding the global minimum.
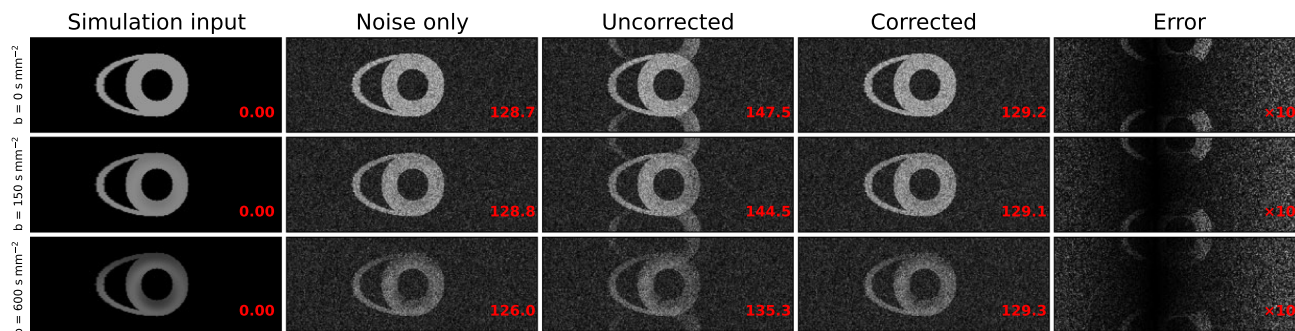
FIGURE 4 An overview of numerical heart phantom simulations. The first column shows the numerical heart phantoms with different diffusion weightings, The middle column shows the simulated data with added noise and ghost. The 4th column shows the corrected image using singular value decomposition-based ghost correction. The rightmost column illustrates the error between the noise-only realization and the corrected image. The magnitude of the error maps are amplified for better visualization. The level of artifact quantified using the magnitude sum of the top 10 and bottom 10 lines from the normalized images are displayed in the bottom right of each subplot.

and FA as a function of SNR in Parts C and D. A systematic bias was introduced by the noise, making the FA progressively overestimated as SNR reduces and causing progressively underestimation of the MD. Nyquist ghost artifacts generally make this bias more severe, particularly at lower SNRs.

An in vivo example of the EPI correction is shown in Figure 7. Upon visual inspection, the navigator approach resulted in significant imaging artifacts for both the SE and STEAM sequences at both low and high b-values. A statistical analysis of the level of artifact over all in vivo datasets was performed using a pairwise comparison between each correction method at each diffusion weightings (Figure 8). All correction methods yielded significant reductions in the level of artifact in comparison to the uncorrected data ($p \ll 0.05$). Among the correction methods, the referenceless methods performed better than the navigator-based method across all diffusion weightings for both sequences, and with p value $\ll 0.05$. However, at high diffusion weighting (specifically at 450 and 600 s mm^{-2}), the referenceless methods struggled to maintain their accuracy, resulting in poorer performance when compared to lower b-values. Nonetheless, even under these challenging conditions, the referenceless methods still outperformed the navigator-based method.

An example of the DT-CMR maps from one subject are shown in Figure 9. All four methods appeared to have similar ghost suppression upon visual inspection. However, a reduction in mean left ventricle MD and an increase in mean FA was observed for referenceless methods, especially for the SE data (Figure 10). As reported by Pierpaoli and Jones,[28,29] any image noise can result in progressively underestimated FA with reducing SNR. The increase in FA after correction is consistent with the increase in SNR of successfully Nyquist ghost corrected diffusion weighted images (Figure 10).

5 | DISCUSSION

B_0 inhomogeneities compromise the performance of the conventional three-line navigator approach, which is typically used for correction of Nyquist ghosts in EPI data. The variation in the B_0 field in the vicinity of the lungs leads to inaccuracies in the phase difference derived from the navigators, resulting in errors in the phase correction process. This issue cannot be remedied by applying an object projection weighted fit to the phase evolution during the fitting process. Our research has demonstrated that, by utilizing a data-driven technique in conjunction with parallel imaging in a DT-CMR study, the Nyquist artifacts are reduced.

It is worth noting that the navigator method has been omitted from our simulation. This omission stems from the fact that a fair simulation of the navigator-based method is inherently complex and simplified simulations would result in an unjust representation of the navigator-based correction. Specifically, simulating three-line navigators from the α and β values (forward model) and subsequently applying a line of best fit to extract the α and β parameters would consistently produce a perfect ghost corrected image, as both images are derived from the same forward model. In order to maintain a fair basis for comparison, it is imperative to keep the forward model and the inverse model entirely independent of each other.

As shown by Figure 3, in cases marked by high SNR, the cost functions exhibit a smooth profile closely resembling the distribution of RMSE. Specifically, both the entropy method and the Ghost/Object method incur higher costs under conditions of elevated β or α values. As the noise level increases, the cost contour plot becomes progressively distorted, yet the region of minimum cost remains situated in the low α and low β
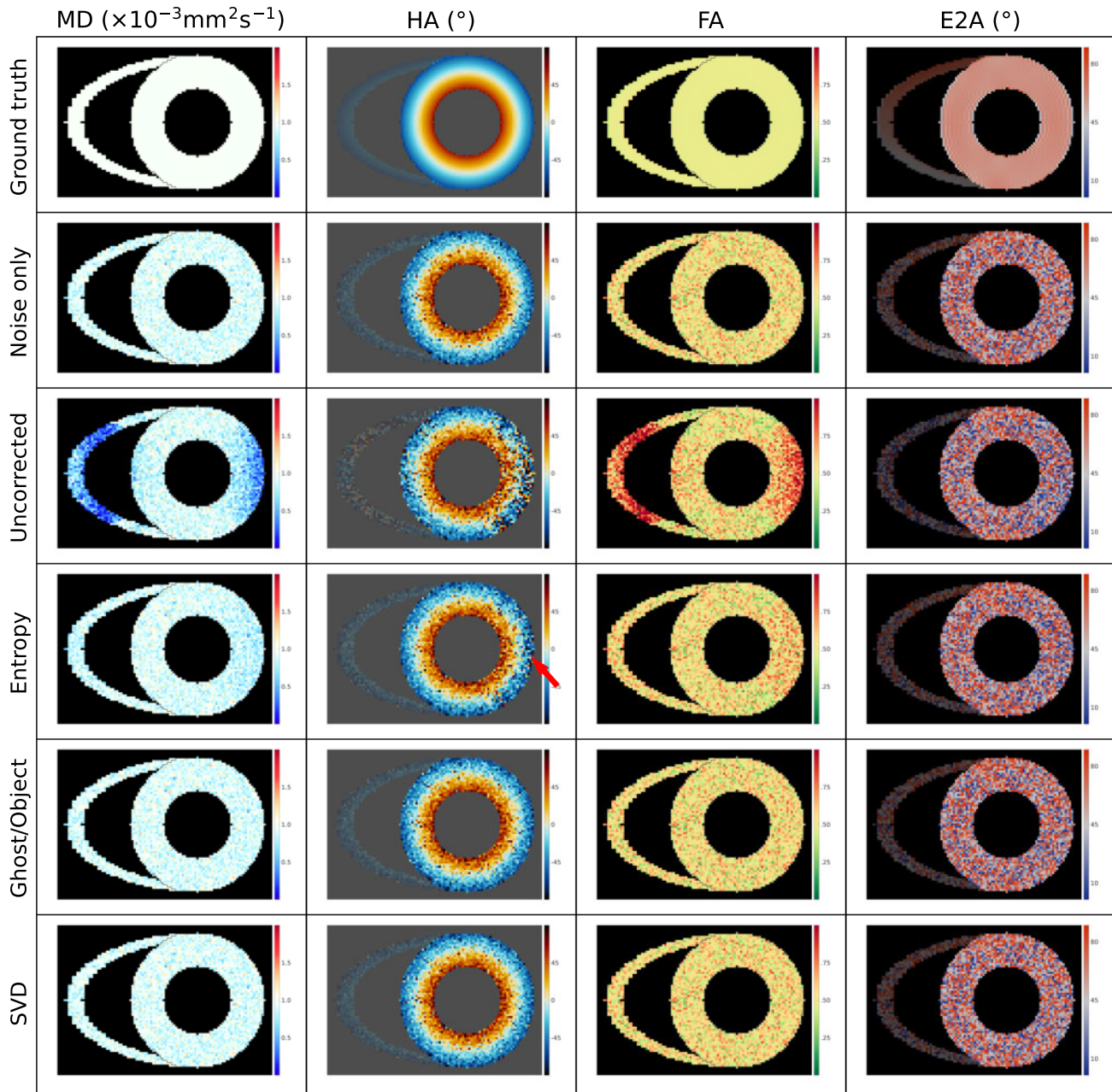
FIGURE 5 An example of the diffusion tensor cardiovascular magnetic resonance maps from the numerical heart phantom simulations. The third row shows the uncorrected case when signal-to-noise ratio is equal to 5. The bottom three rows show the performance of the three referenceless methods for this example.

region. This distortion arises from the noise and the sinusoidal modulation that the α parameter imposed on the ghost and object. The sinusoidal modulations imposed on the ghost and object are out of phase and with higher α values the sinusoidal modulation becomes more pronounced. This makes the cost function lower when considering correlation-based measures like the Ghost/Object cost function. The entropy cost function is harder to interpret, as it treats ghosts with high α and high β as more "detailed" and challenging to compress and hence

in these regions the entropy could be increased. It is important to note that the results are highly dependent on the shape and intensity distribution of the simulated phantoms.

The impact of SNR on ghost correction performance is evident in in vivo experiments when evaluating the ghost correction performance of referenceless methods in both STEAM and SE acquisitions. Notably, the referenceless methods demonstrate superior performance in SE acquisitions compared to STEAM acquisitions, attributed to
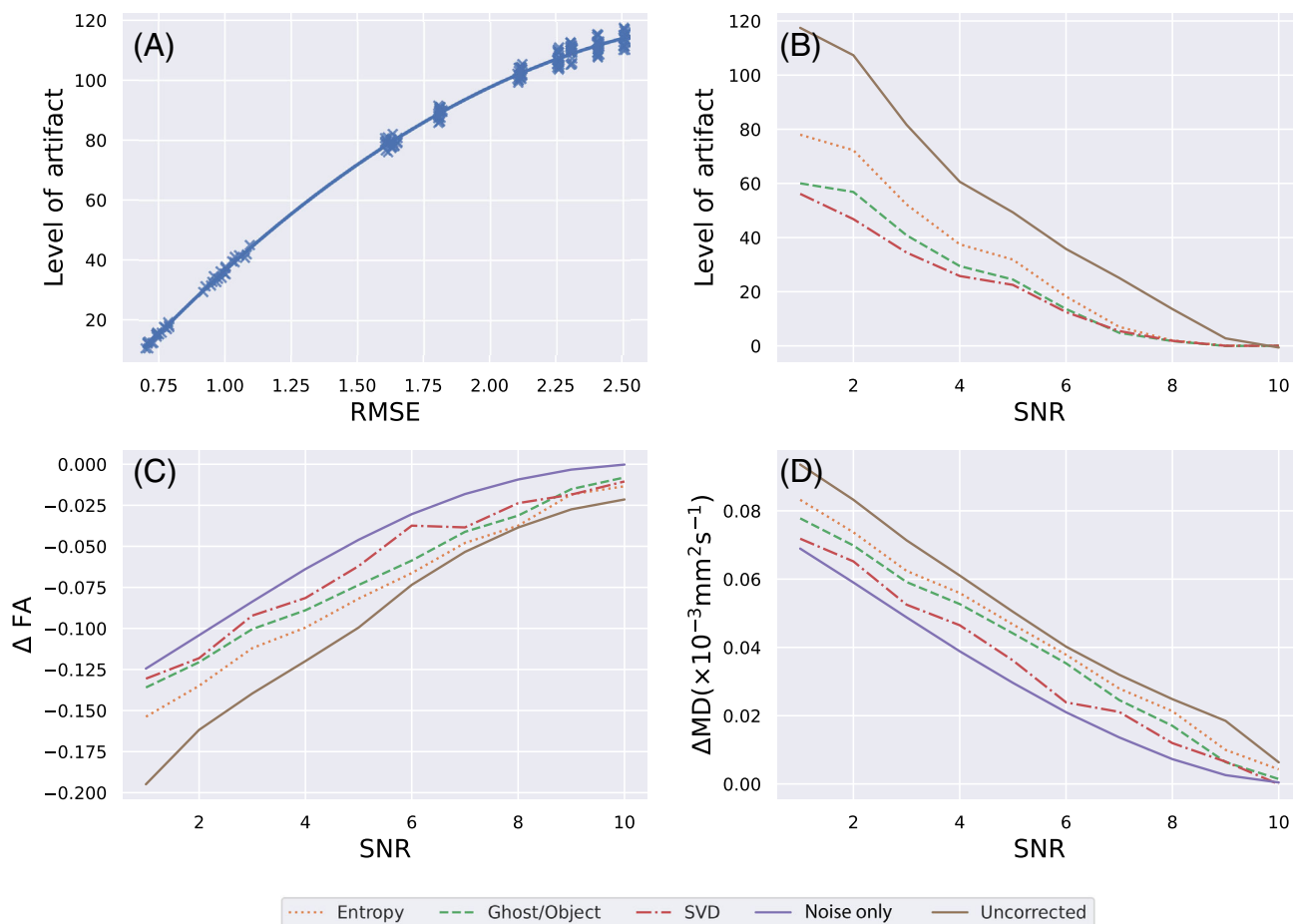
FIGURE 6 The noise sensitivity of all referenceless methods assessed in the numerical phantom. Part (A) demonstrates the feasibility of our proposed Nyquist ghost quantification method using reduced field of view excitation. The root mean square error (RMSE) is computed by measuring the difference between the noise-only realization and the corresponding uncorrected images. The level of artifacts is quantified using the sum of top 10 and bottom 10 lines of the magnitude image. For simplicity, only one realization of α and β is illustrated. To visualize the relationship between these variables, a quadratic function is fitted onto the scatter plot. The quadratic fit is used due to the square root term in the RMSE. Part (B) shows that the level of artifact increases with reduced signal-to-noise ratio (SNR). Part (C) plots the effect of noise on the measurement of mean fractional anisotropy (FA). Part (D) shows the difference in the mean diffusivity (calculated as a mean over the LV) as a function of SNR across all correction methods. As the noise power increased, all methods exhibited progressively increasing systematic biases in FA and mean diffusivity. For reference, parts (C) and (D) also show the effects of noise alone on the FA and MD without the additional Nyquist ghost. The singular value decomposition (SVD) method performs very similarly to the noise only simulations. All statistical results of referenceless methods are bounded within the range defined by the noise-only measurements and the uncorrected data. Note that the eigenvector angle remains relatively unaffected by the presence of noise, and consequently, it is not represented in the depicted plot.

differences in SNR. This assumes that both STEAM and SE acquisitions are affected by similar EPI Nyquist ghosts.

The three unique cost functions used by the referenceless methods represent different strategies for reducing the Nyquist ghosts. The entropy method incorporates image entropy and avoids assumptions regarding the shape or size of the object, however, the outcome may deviate if the search range for the phase offset parameter is too large. In such instances, the algorithm may mistakenly amplify the ghost and try to eliminate the primary object. Thus, the cost function for the Ghost/Object technique might be a more favorable choice, especially in the original

application of the method to breast imaging where a considerable portion of the ghost lies outside the imaged object, as demonstrated in Reference 16. However, the performance of the Ghost/Object overlap measure could be limited by the extent of Object/Ghost overlap in the PE direction. This limitation can be circumvented through the implementation of a reduced FOV technique during data acquisition leaving an object free region at the edge of the FOV. In this case, the image magnitude outside the reduced FOV could serve as an alternative cost function, but may result in inefficiencies in image acquisition. The SVD method relies on the inherent data consistency
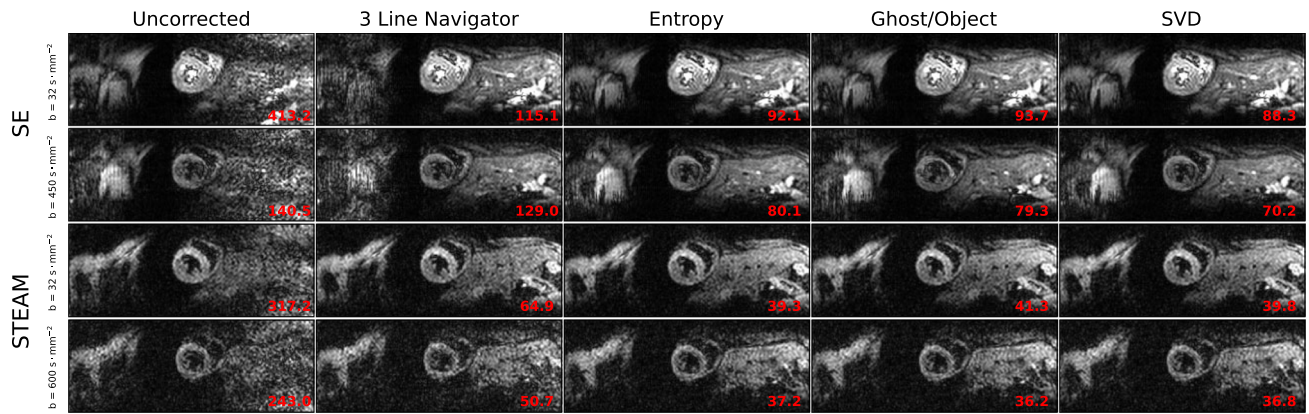
FIGURE 7 Diffusion tensor cardiovascular magnetic resonance (DT-CMR) images acquired in a mid-ventricular short axis slice at peak systole from one example subject. In this example, the referenceless methods show less ghosting than the standard navigator method for both sequences and at all diffusion weightings. More correction examples are included in Figure S1.
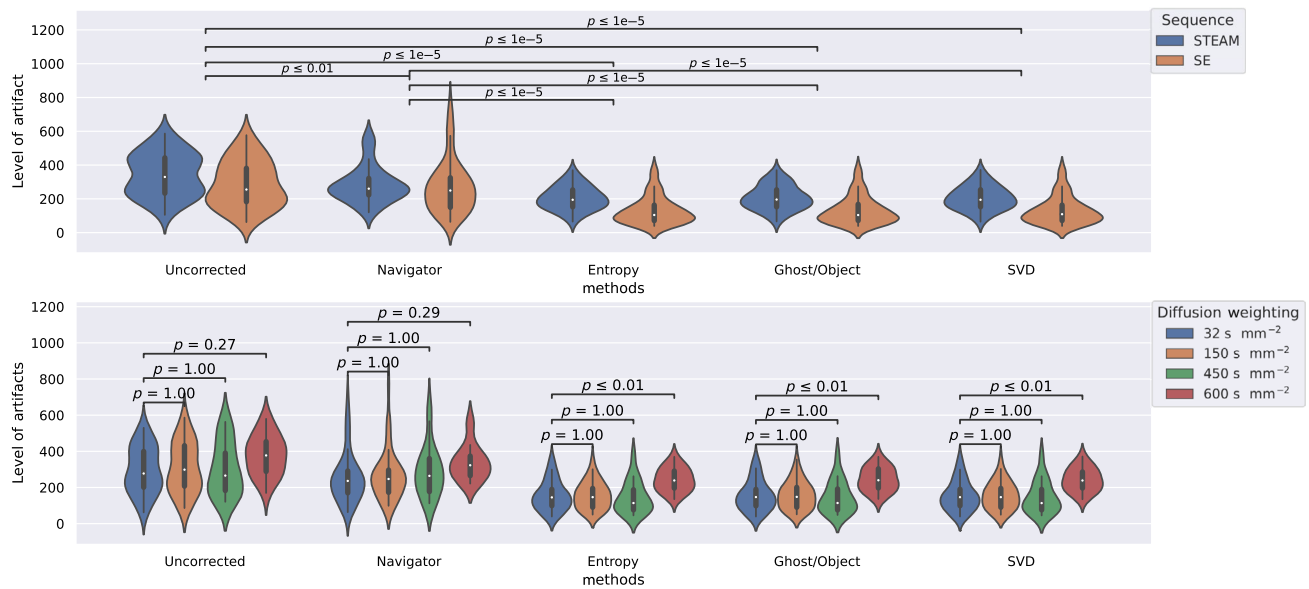

FIGURE 8 Residual ghost intensity across correction methods shown by sequence type and diffusion weighting. The white dot in the middle of the violin plot indicates the median ghost level and the black bar in the center of the violin represents the interquartile range.

between each kernel, and it does not make any a priori assumptions about the structure or contrast of the imaged object. While this approach is effective and robust to noise, addressing higher-order ghosting caused by motion and B_0 inhomogeneity can still be challenging. It is worth noting that the issue of higher order motion-induced ghosting artifacts is not exclusive to the SVD method, but rather a common challenge faced by all other techniques employed in this study.

In approximately 3% of the cases, the referenceless correction methods failed to effectively address the Nyquist ghosting artifacts (detected as outliers in the level of artifact distribution). This highlights the necessity of implementing a more robust method of Nyquist

ghost correction to account for higher-order factors such as motion, eddy currents, and inhomogeneity of the B_0 field (one instance of an unsuccessful referenceless-based correction is illustrated in Supporting Figure S2). The navigator-based approach offers the potential to extend to higher-order correction with only minimal increases in computational requirements. Although all the referenceless methods explored in this study can be adapted to accommodate higher-order correction, it should be noted that the computational time will rapidly increase. Despite this limitation, we chose to limit our comparison to linear correction as is typical for EPI Nyquist ghost correction and does provide good ghost correction in a the vast majority of cases.
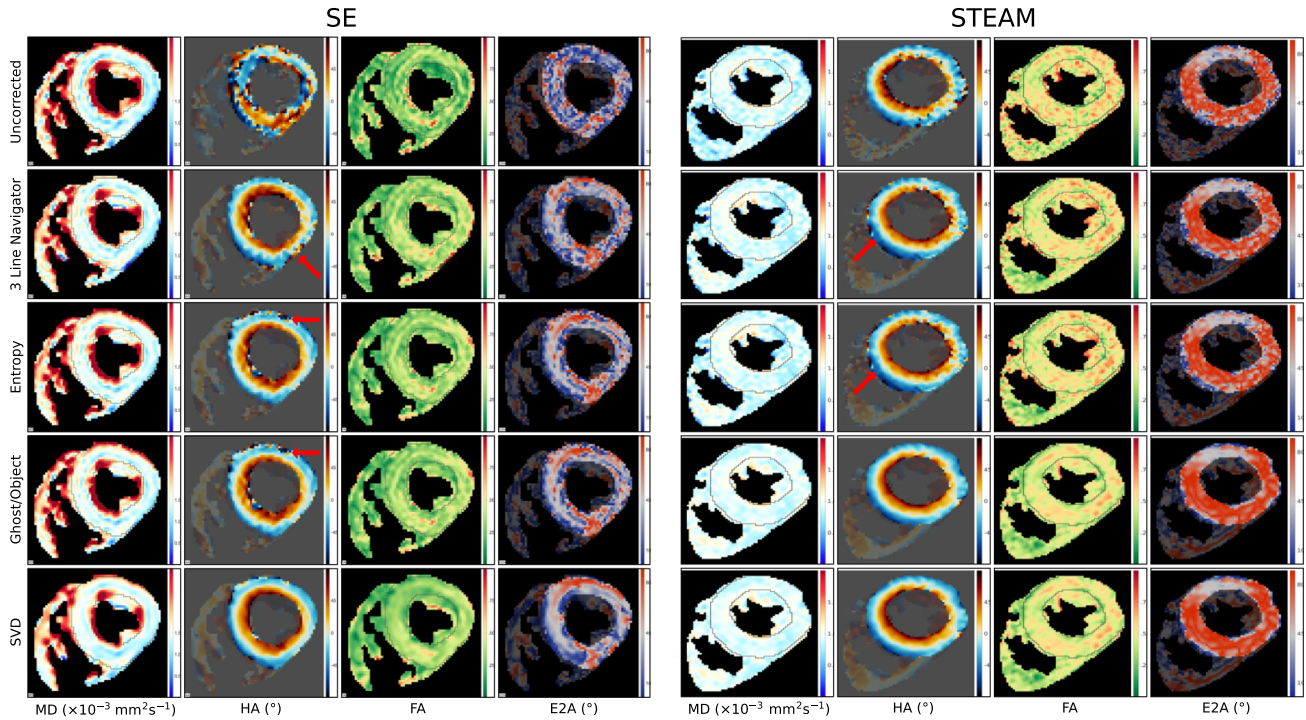
FIGURE 9 Example of the diffusion tensor cardiovascular magnetic resonance (DT-CMR) maps from one health subject for spin echo (SE) and STEAM with diffusion correction methods, including mean diffusivity (MD), helix angle (HA), fractional anisotropy (FA), and second eigenvector angle (E2A). Despite the reduction in acquisition time, the referenceless methods resulted in visually better image quality than the navigator-based correction. Note that different subjects were used for SE and STEAM to highlight the difference between the DT-CMR map outcomes resulting from various correction methods.
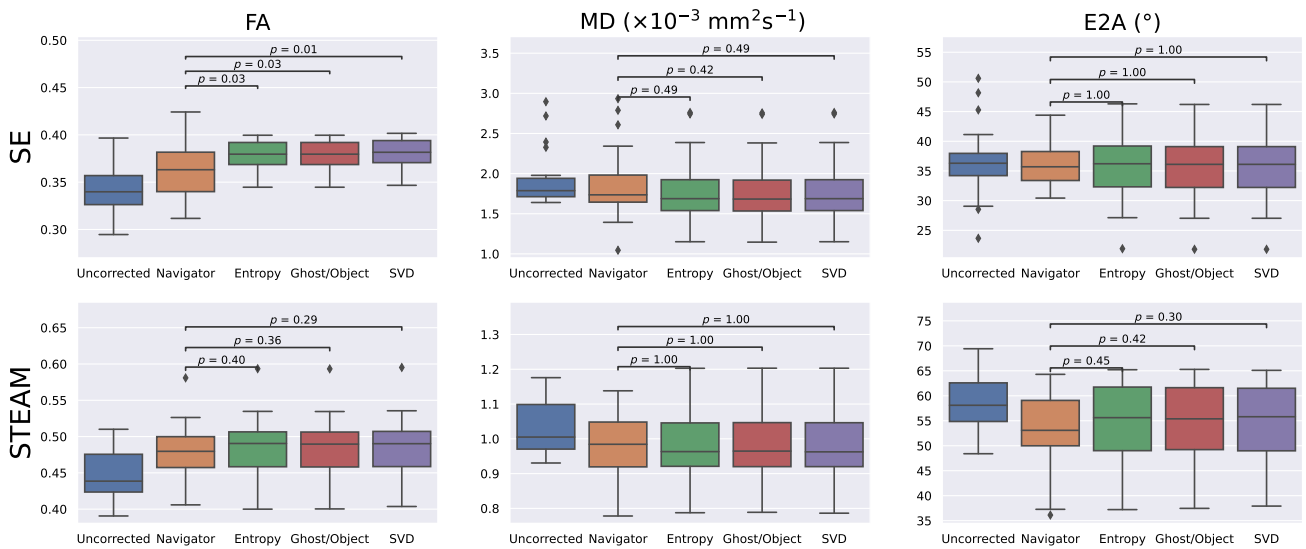

FIGURE 10 Diffusion tensor cardiovascular magnetic resonance results for all subjects: mean left ventricle mean diffusivity (MD), mean fractional anisotropy (FA), and the median of the absolute value of E2A. The referenceless methods result in a reduction in MD and increase in FA particularly for the spin echo data.

Within a conventional DT-CMR imaging breath hold, a total of nine imaging datasets are acquired. This set comprises one EPI navigator scan, one parallel imaging reference scan, followed by seven DT-CMR scans. With

a TR of two cardiac cycles, the data acquisition spans 18 cardiac cycles. It is imperative that the phase error in all EPI scans align precisely with that of the EPI navigator scan. Any deviation in this alignment will lead to residual

Nyquist ghosts. Such discrepancies may arise due to factors such as patient motion when sampling the EPI navigator. However, the navigator method boasts a key advantage of being independent of the diffusion encoding and image SNR. The navigators are acquired prior to the application of the diffusion gradients, rendering them immune to the negative effects of eddy currents. In contrast, reference-less methods can be impacted by the decrease in image SNR caused by the high strength of diffusion gradients, such as those seen with b-values of 450 and 600 s mm^{-2}. This can result in suboptimal Nyquist ghost correction parameters. However, it has been demonstrated that referenceless methods still outperform navigator-based methods across all diffusion encoding schemes and sequences tested, despite the lower SNR at higher diffusion weighting.

The Nyquist ghost artifact can affect the accuracy of DT-CMR maps by introducing spatial variations in the image data either from shifted replicas or a cosine modulation or both. The presence of uncorrected Nyquist ghosts may give rise to a global reduction in FA, potentially resulting in erroneous disease indications. In this work, an average coil, per shot, per slice, and per acquisition correction was used to effectively suppress the Nyquist ghost artifact, even with low SNR. To minimize the detrimental effects of low SNR with data-driven techniques, we used coil combined images to evaluate the cost functions in order to perform averaged-coil correction rather than correcting on a per-coil basis. The per-coil correction method exhibits the capability to accommodate variations in the ghost parameters between coils. However, this method is susceptible to errors, which can result in biased ghost estimation (see Supporting Figure S3). When using the averaged-coil correction with referenceless methods, the SNR can be notably enhanced, thus significantly improving the results and outweighing its limitations as an averaged-coil correction.

Referenceless techniques, though effective, are known to be computationally intensive, requiring more calculation time than traditional navigator methods. When implementing the algorithms on central processing units, the SVD method is considered the most time-consuming among the referenceless techniques (averaging around 14 min per subject), taking about 10 times longer than the Ghost/Object Minimization approach (1.4 min) and 12 times longer than the Entropy-based method (1.2 min). To tackle this issue, the SVD method was implemented on a graphics processing unit, which resulted in a substantial increase in speed, with a seven-fold acceleration compared to the central processing unit implementation, averaging around 2 min.

As outlined in the Ghost/Object Minimization approach, when applying in-plane parallel imaging, a second iteration of correction is necessary for dynamic correction.[16] This includes performing GRAPPA or SENSE reconstruction at each point in the 2D search space, which can range from 1000 to 10 000 reconstructions, depending on the density of the search space. Hence, it is advisable to utilize graphics processing unit processing and parallel computing for practical clinical implementation. However, it was noted in our in vivo experiments that phase errors tend to vary only slightly for a given subject. As a result, a single, detailed search may be sufficient for the first repetition, and the search space can be significantly reduced for subsequent acquisitions.

The use of referenceless methods in DT-CMR is especially beneficial given the available imaging window is fixed and repetition time is constrained by the RR interval of the subject. This typically leads to prolonged data acquisitions. The referenceless methods can save valuable imaging time and, for example, in a typical protocol used in clinical DT-CMR research, the time saved could be used to acquire an additional signal average or diffusion encoding direction. In addition, referenceless methods do not rely on coil sensitivity profiles, making them compatible with a wide range of parallel imaging techniques and simultaneous multislice applications.[25,27,30]

6 | CONCLUSION

Our study demonstrates that referenceless methods outperform navigator-based approaches in correcting Nyquist ghosts in DT-CMR settings. These methods show promise in providing accurate and reliable Nyquist corrections, while also providing significant time savings by eliminating the need for additional reference scans. Therefore, the adoption of these referenceless methods has the potential to enhance the efficiency and dependability of DT-CMR measurements in future clinical research studies and eventually clinical routine.

CONFLICT OF INTEREST STATEMENT
Radhouene Neji and Karl Kunze are employees of Siemens Healthcare.

ORCID
Zimu Huo https://orcid.org/0009-0008-3426-326X
Ke Wen https://orcid.org/0009-0005-4313-8469
Yaqing Luo https://orcid.org/0009-0003-2140-141X
Radhouene Neji https://orcid.org/0000-0002-6543-4390

Pedro F. Ferreira 🔵 https://orcid.org/0000-0002-0436
-3496
Dudley J. Pennell 🔵 https://orcid.org/0000-0001-5523
-1314
Andrew D. Scott 🔵 https://orcid.org/0000-0001-7656-3123
Sonia Nielles-Vallespin 🔵 https://orcid.org/0000-0003
-0412-2796

REFERENCES

1. Nielles-Vallespin S, Scott A, Ferreira P, Khalique Z, Pennell D, Firmin D. Cardiac diffusion: technique and practical applications. *J Magn Reson Imaging*. 2019;52:348-368.
2. Heid O. Robust EPI phase correction. 1997.
3. Scott AD, Nielles-Vallespin S, Ferreira PF, McGill LA, Pennell DJ, Firmin DN. The effects of noise in cardiac diffusion tensor imaging and the benefits of averaging complex data. *NMR Biomed*. 2016;29:588-599.
4. Wang FN, Huang TY, Lin FH, et al. PROPELLER EPI: an MRI technique suitable for diffusion tensor imaging at high field strength with reduced geometric distortions. *Magn Reson Med*. 2005;54:1232-1240.
5. Hu X, Le TH. Artifact reduction in EPI with phase-encoded reference scan. *Magn Reson Med*. 1996;36:166-171.
6. Chen NK, Wyrwicz AM. Removal of EPI Nyquist ghost artifacts with two-dimensional phase correction. *Magn Reson Med*. 2004;51:1247-1253.
7. Buonocore MH, Gao L. Ghost artifact reduction for echo planar imaging using image phase correction. *Magn Reson Med*. 1997;38:89-100.
8. Xiang QS, Ye FQ. Correction for geometric distortion and N/2 ghosting in EPI by phase labeling for additional coordinate encoding (PLACE). *Magn Reson Med*. 2007;57:731-741.
9. Lee J, Jin KH, Ye JC. Reference-free single-pass EPI Nyquist ghost correction using annihilating filter-based low rank Hankel matrix (ALOHA). *Magn Reson Med*. 2016;76:1775-1789.
10. Xie VB, Lyu M, Liu Y, Feng Y, Wu EX. Robust EPI Nyquist ghost removal by incorporating phase error correction with sensitivity encoding (PEC-SENSE). *Magn Reson Med*. 2017;79:943-951.
11. Hoge WS, Polimeni JR. Dual-polarity GRAPPA for simultaneous reconstruction and ghost correction of echo planar imaging data. *Magn Reson Med*. 2015;76:32-44.
12. Kim YC, Nielsen JF, Nayak KS. Automatic correction of echo-planar imaging (EPI) ghosting artifacts in real-time interactive cardiac MRI using sensitivity encoding. *J Magn Reson Imaging*. 2008;27:239-245.
13. Kellman P, McVeigh ER. Phased array ghost elimination. *NMR Biomed*. 2006;19:352-361.
14. Li H, Fox-Neff K, Vaughan B, French D, Szaflarski JP, Li Y. Parallel EPI artifact correction (PEAC) for N/2 ghost suppression in neuroimaging applications. *Magn Reson Imaging*. 2013;31:1022-1028.
15. Clare S. Iterative Nyquist ghost correction for single and multi-shot EPI using an entropy measure. Paper presented at: Proceedings of ISMRM, Toronto, Canada, 2003.
16. McKay JA, Moeller S, Zhang L, Auerbach EJ, Nelson MT, Bolan PJ. Nyquist ghost correction of breast diffusion weighted imaging using referenceless methods. *Magn Reson Med*. 2018;81:2624-2631.
17. Clare S. A fast and robust minimum entropy based non-interactive Nyquist ghost correction algorithm. Paper presented at: Proceedings of ISMRM, Miami, Florida. 2005.
18. Peterson E, Aksoy M, Maclaren J, Bammer R. Acquisition-free Nyquist ghost correction for parallel imaging accelerated EPI. Paper presented at: Proceedings of ISMRM, Miami, Florida. 2005.
19. Nielles-Vallespin S, Mekkaoui C, Gatehouse P, et al. In vivo diffusion tensor MRI of the human heart: reproducibility of breath-hold and navigator-based approaches. *Magn Reson Med*. 2013;70:454-465.
20. Scott AD, Nielles-Vallespin S, Ferreira PF, et al. An in-vivo comparison of stimulated-echo and motion compensated spin-echo sequences for 3 T diffusion tensor cardiovascular magnetic resonance at multiple cardiac phases. *J Cardiovasc Magn Reson*. 2018;20:1.
21. Bernstein M, King K, Zhuo X. Chapter 16 – Echo train pulse sequences. In: Bernstein M, King K, Zhuo X, eds. *Handbook of MRI Pulse Sequences*. Academic Press; 2004:702-801.
22. Shannon C. A mathematical theory of communication. *Bell Syst Tech J*. 1948;27:379-423.
23. Shin PJ, Larson PE, Ohliger MA, et al. Calibrationless parallel imaging reconstruction based on structured low-rank matrix completion. *Magn Reson Med*. 2014;72:959-970.
24. Heinig G, Jankowski P. Kernel structure of block Hankel and Toeplitz matrices and partial realization. *Linear Algebra Appl*. 1992;175:1-30.
25. Setsompop K, Gagoski BA, Polimeni JR, Witzel T, Wedeen VJ, Wald LL. Blipped-controlled aliasing in parallel imaging for simultaneous multislice echo planar imaging with reduced g-factor penalty. *Magn Reson Med*. 2011;67:1210-1224.
26. Fessler J. Michigan image reconstruction toolbox (MIRT). https://github.com/JeffFessler/mirt. Accessed February 3, 2021
27. Griswold MA, Jakob PM, Heidemann RM, et al. Generalized autocalibrating partially parallel acquisitions (GRAPPA). *Magn Reson Med*. 2002;47:1202-1210.
28. Pierpaoli C, Basser PJ. Toward a quantitative assessment of diffusion anisotropy. *Magn Reson Med*. 1996;36:893-906.
29. Jones DK, Basser PJ. Squashing peanuts and smashing pumpkins: how noise distorts diffusion-weighted MR data. *Magn Reson Med*. 2004;52:979-993.
30. Setsompop K, Cohen-Adad J, Gagoski BA, et al. Improving diffusion MRI using simultaneous multi-slice echo planar imaging. *Neuroimage*. 2012;63:569-580.

SUPPORTING INFORMATION

Additional supporting information may be found in the online version of the article at the publisher's website.

Figure S1. Additional in vivo reconstruction examples using the navigator and referenceless methods. Part (A) demonstrates an unsuccessful correction using the navigator method. Part (B) showcases the typical performance of reconstructions achieved through both navigator and referenceless methods. Part (C) exhibits all reconstruction methods achieving similarly high-quality ghost performance. In general, referenceless methods outperformed navigator-based method in our study.

Figure S2. An instance of an unsuccessful referenceless correction. To aid visualization of the Nyquist ghosting, the images were thresholded. The cost function was calculated for every possible combination of the candidate Nyquist ghost correction parameters and displayed as a contour plot. The solution for each method is plotted as a red dot. To facilitate comparison between different methods, the cost function values were normalized to a range between 0 and 1. Although all referenceless methods reached a minimum, strong residual ghosts were still observed. The cause of this residual Nyquist ghosting could be attributed to two main factors. Firstly, if motion is present during the scan, there could be a mismatch between the phase difference extracted from the fully sampled calibration signal and the actual under-sampled data. Secondly, higher order Nyquist ghost can be introduced by motion, eddy currents, and inhomogeneity of the B0 field, and a simple linear fit is not able to fully capture the Nyquist ghost present on the image.

Figure S3. A comparison of EPI phase navigator signals using averaged-coil correction and per-coil correction. The Savitzky-Golay filter is applied on the extracted phase difference (blue), and fit to a linear ghost correction model (orange) weighted by the 1D object projection (red). The per-coil linear fit appears to be nosier than that of the averaged-coil method, highlighted by the difference in the slope of the extracted phase profile. While the per-coil correction accounts for coil-to-coil variation, it may also introduce bias due to noise and coil specific phase error due to eddy currents. In this example, our results show that the per-coil phase correction can lead to a bias in the linear phase estimate for coil 7, resulting in unresolved ghosting.